In-cloud processing as a possible source of isotopically light iron from anthropogenic aerosols: New insights from a laboratory study

Daniel Santos Mulholland, Pascal Flament, Jeroen de Jong, Nadine Mattielli, Karine Deboudt, Guillaume Dhont, Eugène Bychkov

IN-CLOUD PROCESSING AS A POSSIBLE SOURCE OF ISOTOPICALLY LIGHT IRON FROM ANTHROPOGENIC AEROSOLS: NEW INSIGHTS FROM A LABORATORY STUDY

Daniel Santos Mulholland[1,3*], Pascal Flament[1], Jeroen de Jong[2], Nadine Mattielli[2], Karine Deboudt[1], Guillaume Dhont[1] and Eugène Bychkov[1]

[1]*Laboratoire de Physico-Chimie de l'Atmosphère, Université du Littoral Côte d'Opale, Dunkerque, France*

[2]*Laboratoire G-Time, Université Libre de Bruxelles (ULB), Brussels, Belgium*

[3]*Laboratório de Análises Ambientais – Química Ambiental, Universidade Federal do Tocantins, Gurupi, Tocantins, Brasil*

*Corresponding Author:

Laboratório de Análises Ambientais - Química Ambiental

Universidade Federal de Tocantins, Rua Badejós, Lote 7, Chácaras 69/72

Gurupi (TO) Brazil, 77402-970

ORCID ID: 0000-0001-9739-842X

Abstract

Wet atmospheric deposition can account for up to 50% of the total iron input to surface waters, so establishing the extent to which kinetic and equilibrium isotope effects can influence aerosol soluble $\delta^{56}Fe$ values is imperative to trace and constrain aerosol sources using Fe isotopes and to understand the differences found between $\delta^{56}Fe$ values for bulk and soluble phases of aerosols. In this context, changes in iron solubility and isotopic composition of dissolved Fe during simulated atmospheric processing of industrial ash was investigated. Kinetic and equilibrium experiments were performed under UV/VIS light using ash from a Fe–Mn alloy metallurgical plant and a synthetic solution that mimics cloud water chemistry. The nature of the Fe species of the industrial ash was investigated by Mössbauer Spectroscopy, whereas ash and dissolved $\delta^{56}Fe$ values were measured by MC-ICP-MS. Mössbauer Spectroscopy revealed that α-hematite, magnetite, and poorly crystallized manganoferrite nanoparticles are the main Fe species. In the early-stage dissolution (until 60 min) a Fe isotope fractionation ($\Delta^{56}Fe_{solution\text{-}bulk\ ash}$) of -0.284 ± 0.103‰ was found at the minimum contact time evaluated herein (i.e., 5 min.) due to kinetic isotopic effects. In the late-stage dissolution (after 60 min) a $\Delta^{56}Fe_{solution\text{-}ash}$ of 0.227 ±0.091‰ was found due to equilibrium isotopic effects. The kinetic isotope effect within one ash surface monolayer was modeled with an enrichment factor (ε) of -1‰ in $^{56}Fe/^{54}Fe$ ratio. Iron fractional dissolution undergone during different atmospheric processing time scales may release Fe with contrasted isotope compositions to solution, changing the original soluble Fe isotope signature (which is linked to its source). This might be especially important when the dissolution process goes from kinetic to near-equilibrium conditions, in which higher amounts of Fe are progressively released from ash surface.

Keywords: iron isotope; iron dissolution; aerosol; cloud processing; isotope fractionation; iron oxide

Graphical Abstract

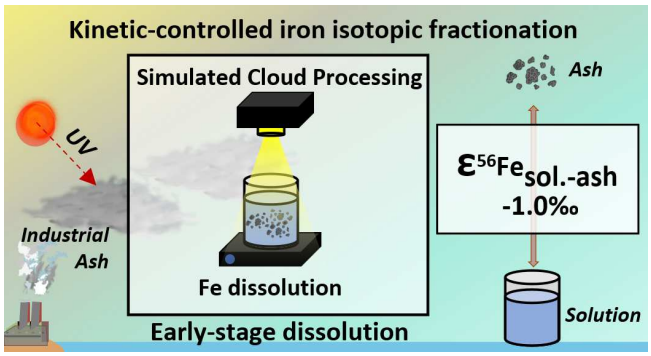

1. INTRODUCTION

Iron is a key micronutrient that limits primary productivity over vast areas of oceans due to its low solubility in seawater and, therefore, it has strongly impacted the world's fixation of carbon dioxide (Field et al., 1998; Boyd and Ellwood, 2010; Tagliabue et al., 2017) and global nitrogen fixation (Geider and La Roche, 1994). Iron is added to oceans by three main pathways known as margin sediment dissolution, atmospheric dust dissolution, and hydrothermal dispersion (e.g., Jickells et al., 2005; Tagliabue et al., 2010; Radic et al., 2011). Regionally variable dust from arid and semi-arid regions dominates the global total Fe aeolian dust cycle and has long been considered as an important external input of Fe source to the ocean's surface waters (Mahowald et al., 2005), particularly in regions such as the North Atlantic due to its proximity to the Saharan dust source (Conway and John, 2014). Recent studies showed that noncrustal sources arising from anthropogenic activities such as industrial emissions and fossil, biofuel and biomass burning (i.e. pyrogenic particles) emissions may also be important Fe sources, especially due to their high soluble Fe concentrations (e.g., Sedwick et al., 2007; Luo et al., 2008; Sholkovitz et al., 2009; Ito et al., 2019; Rodríguez et al., 2021 and references therein). Anthropogenic Fe-bearing aerosols display solubility several orders of magnitude higher than the primary natural source of atmospheric Fe to oceans (Sedwick et al., 2007). Therefore, variations in the atmospheric soluble Fe input into the oceans induced by anthropogenic activities likely exert strong influence on marine phytoplankton carbon uptake and storage, playing an important role in the global CO_2 budget and eventually in climate change (Kohfeld et al., 2005; Martínez-Garcia et al., 2011).

To provide a reliable mass balance of reactive Fe in the global ocean, the isotope fingerprint technique might be relevant if the isotope composition of the sources and the process undergone in the aerosol atmospheric lifetime have been well addressed (Chen et al., 2020). Bulk natural aerosol dust has been assigned to yield a near-crustal δ^{56}Fe value of +0.1‰ (Poitrasson, 2006; Waeles et al., 2007; Mead et al., 2013), whereas the Fe isotope compositions of anthropogenic endmembers are

highly fractionated with δ^{56}Fe values ranging from -3 to +0.3‰ (Majestic et al., 2009; Mead et al., 2013; Kurisu et al., 2016a, 2016b). Recent studies linked aerosols yielding light δ^{56}Fe values with an anthropogenic component (*e.g.*, Kurisu et al., 2016; Conway et al., 2019) based on their proximity to combustion sources (Majestic et al., 2009; Mead et al., 2013; Kurisu et al., 2016). While these light isotope signatures can be linked to a primary anthropogenic source, the presence of a lighter-than-bulk soluble δ^{56}Fe may also be indicative of kinetic isotope effects undergoing Fe partial dissolution during atmospheric processing (Revels et al., 2015; Chen et al., 2020).

Iron isotopes are known to fractionate through kinetic and equilibrium effects in earth surface low temperature environments (Beard, 2003; Wiesli et al., 2004) and might be a prominent tool to better understand the aqueous-phase reactions between aerosol Fe and cloud water. Previous studies (Wiederhold et al., 2006; Chapman et al., 2009; Kiczka et al., 2010) showed that ligand-promoted and reductive dissolution of goethite and silicates caused the preferential release of isotopically light Fe in the early fraction released from the mineral surface, due to kinetic isotope effects undergone in early-stage dissolution. Together with proton-promoted dissolution, these processes are among the most relevant mechanisms that enhance solubility of Fe-bearing aerosol particles during cloud processing (Chen and Grassian, 2013). Therefore, establishing the extent to which kinetic and equilibrium isotope effects can influence aerosol soluble δ^{56}Fe values is imperative to trace and constrain aerosol sources using Fe isotopes, and understand the differences between δ^{56}Fe values found for bulk and soluble phases of aerosols, such as those reported for near-source aerosols found at Hiroshima, Japan (Kurisu et al., 2016) and open ocean North Atlantic airborne particles (Conway et al., 2019). This is all the more necessary since wet atmospheric deposition can account for up to 50% of the total iron input to surface waters, for example in the subtropical North Atlantic (López-García et al., 2021).

The present study investigated changes in iron solubility and dissolved Fe isotopic composition leached from pyrogenic particles (an industrial ash collected from a Fe-Mn alloy company), during

simulated atmospheric processing using leaching solutions that mimic cloud water chemistry. The "coke + ore" sintering process is widespread in the field of metallurgy and in the iron and steel industry and the particles emitted are therefore representative of the emissions of this type of production unit which is, moreover, known to be the most emissive among all the units constituting a metallurgy or iron and steel plant. Lab-scale experiments were performed aiming to: (*i*) evaluate the kinetic and equilibrium mechanisms involved in Fe dissolution; (*ii*) understand the effect of dissolution on the isotopic composition of the remaining dissolved Fe phase; and (*iii*) understand the mechanisms controlling Fe isotopic fractionation during cloud processing experiments. The results reported herein can be used to better understand the integrated in-cloud chemical processes during atmospheric transport of aerosols collected in different Earth surface pools and support the identification of possible sources of the airborne particles.

2. MATERIAL AND METHODS

2.1. Nature of the industrial ash particles

The industrial ash used by the present study belongs to a Fe – Mn alloy metallurgical plant located at Dunkerque in northern France. The particles were collected in the chimney filter of the industry sintering working unit where the raw ore is transformed into an intermediate grade material using anthracite as the reducing agent (Marris et al., 2013). The industrial ash consists of a mixture of metallic, aluminosilicate and aluminosilicate-metallic particles (irrespective of their sizes), containing approximately 76-89% of Mn oxides (Marris et al., 2013) and 6.2 wt.% of Fe (Table S1 in Supplementary Material).

2.2. Synthetic cloud water composition

Iron dissolution experiments were performed using solutions that mimic cloud water chemical composition to simulate the atmospheric aerosol dissolution processes as closely as possible. The

concentrations of dissolved major ions (Ca^{2+}, Mg^{2+}, NH_4^+, K^+, Na^+, Cl^-, NO_3^-, and SO_4^{2-}), and organic compounds (formate, acetate, oxalate, malonate, and tartrate) were set in agreement with average values calculated from cloud water composition collected in different regions worldwide, as reported by Guo et al. (2012), Paris and Desboeufs (2013) and the references therein. Synthetic cloud water solutions were prepared using reagents of analytical grade and ultrapure water (≥18.2 MΩ cm). The synthetic cloud water was prepared using NaCl, $CaSO_4$, $Mg(NO_3)_2.6H_2O$, KNO_3, $CH_3CO_2NH_4$, $CH_3CO_2NH_4$ and HCO_2NH_4 Merk Suprapur® salts, and HCl, HNO_3 and H_2SO_4 distilled acids, which were also applied to decrease solution pH. The concentrations of the inorganic compounds introduced in the synthetic cloud water were verified by Ionic Chromatography using a Dionex ICS-5000 Ion Chromatography System, whereas the concentrations of the organic compounds were estimated through stochiometric calculations. The measured and estimated concentrations of the synthetic cloud water used herein are shown in Tables S2 and S3. Before starting the experiments, solution pH was adjusted to 2 using few drops of conc. $HClO_4$, since perchlorates are a weak ligand capacity in low ionic strength solutions (Johansson and Yokoyama, 1990) and do not form Fe complexes.

2.3. Iron dissolution experiments

The Fe dissolution experiments performed under UV/VIS irradiation evaluated herein were similar to that of Wiederhold et al. (2006), but to be representative of the dissolution mechanisms occurring during the atmospheric transport of pollution aerosols, the concentration range of organic ligands was adjusted to values commonly found in cloud waters and the experiment duration was adapted to the lifetime of cloud droplets, i.e. a few hours (Flossmann and Wobrock, 2019). A maximum ash and solution contact time of 120 min was established, since it is consistent with aerosol processing between cloud droplet formation and precipitation (Warneck, 1988) and agrees with the dissolution time performed by previous studies (e.g., Paris and Desboeufs, 2013). The ash

concentration was defined according to preliminary dissolution experiments that showed faster dissolution rates and higher final dissolved Fe concentrations in more acidic solutions with an ash concentration of 250 mg/L (Figure 1a,b). A higher ash concentration (1000 mg/L) possibly created experimental or filtration artifacts and reduced Fe solubility towards higher contact times (Figure 1b). The dissolution experiments performed to evaluate iron isotope fractionation used pH 2 synthetic cloud water solutions with an ash concentration of 250 mg/L to improve signal intensity during Fe isotope measurements due to the higher concentration of dissolved Fe in the final solution (Figure 1a). The dust concentrations reported herein were in agreement with those found in cloud water, which usually range from 100 µg/L to 1 g/L (Shi et al., 2012 and references therein).

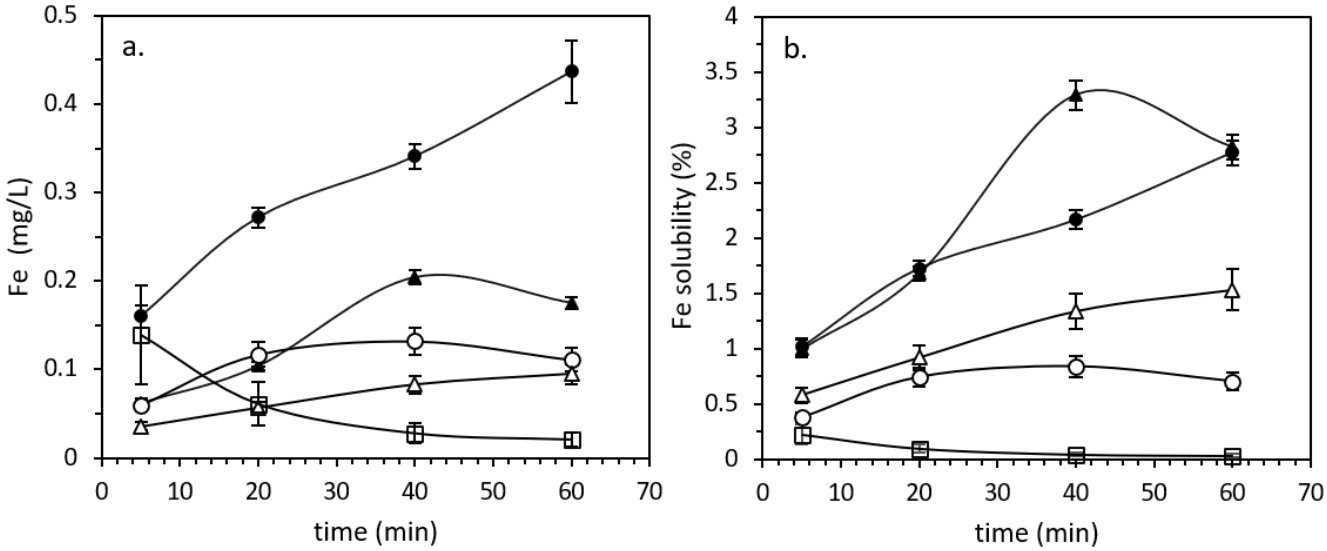

Figure 1: Dissolved Fe concentrations (a) and Fe solubility (b) during simulated atmospheric processing of industrial ash in pH 2 solutions (black circles and triangles) and pH 3 solutions (open circles, triangles, and squares) with industrial ash concentrations of 100 mg/L (black and open triangles), 250 mg/L (black and open circles), and 1000 mg/L (open squares). Error bars represent two standard deviations (± 2SD) of the experimental data.

Independent experiments were conducted in Savillex® Teflon vessels during a contact time between ash and solutions of 5, 30, 60, 90 and 120 min at ~25° C with constant UV/VIS irradiation promoted by a Newport® Oriel Sol1A, Class ABB solar simulator. An amount of 7 mg of industrial ash was precisely weighted on a previously 1M HCl cleaned plastic weighing boat using a Metller

175 Toledo microbalance (XP6 model). The ash was transferred to a 30 mL Savillex Teflon vessel
176 containing 23 mL of synthetic cloud solution and the weighing boat was rinsed with 5 mL of
177 synthetic cloud water to ensure that all ash particles were transferred to the Teflon vessel, making up
178 a final volume of 28 mL and an ash concentration of 250 mg/L. The Savillex was immediately
179 placed over a magnetic stirrer under constant UV/VIS irradiation. After the predefined contact time,
180 the vessel was removed from the stirrer and the solution was immediately filtered using a Millipore
181 cellulose acetate membrane with 0.45 µm pore size previously rinsed with 2% HNO_3. Aliquots of ≈
182 10 and 20ml of the filtered solution were acidified using conc. HNO_3 for further Fe concentration
183 and isotopic composition measurements, respectively. Analysis of the cloud water showed it had an
184 Fe concentration of 4.2 µg/L, which is less than 3% of the minimum amount of dissolved Fe
185 measured in samples collected from the dissolution experiments. To verify the reproducibility of the
186 results, the experiments were performed three times. Control experiments were performed to
187 investigate the role of colloidal Fe in the dissolved Fe isotope signature and evaluated possible Fe
188 precipitation. These independent dissolution experiments were performed with the same solution pH,
189 ash concentration and duration as the ones performed for isotope measurements, but the final
190 solutions were first filtered with membranes with 0.45 µm pore size and subsequently filtered with a
191 Macrosep Centrifugal Filter with 100 KDa pore size. Iron concentrations measured in the <0.45µm
192 and <100KDa fractions were identical. Images from the 100KDa membranes performed by Scanning
193 Electron Microscopy did not show colloidal Fe phases. Together, these observation showed that Fe is
194 mainly present as truly dissolved metal, due to the acidic solution pH, and complexed with organic
195 ligands, e.g. $Fe(C_2O_4)_n$ due to the presence of oxalate.
196
197 *2.4. Mossbauer Spectroscopy*
198 The typical room-temperature ^{57}Fe Mössbauer spectrum of industrial ash particles is shown in
199 Figure 2. The spectrum shows a quadrupole doublet (i) and at least three magnetically-split Zeeman

patterns (ii), corresponding to the Fe(III) ions and the iron oxide form, respectively. The results of a least-square fit using the Lorentzian line shape are collected in Table S4 in SI. These paramagnetic (i) and magnetically (ii) forms are present in comparable proportions, *i.e.,* 47.7% and 52.3%, respectively. The isomer shifts IS are given relative to α-Fe, and the quadrupole splitting QS, hyperfine magnetic field H_{eff} and line width W are also shown. The sextet with the largest H_{eff} = 51.4 T (red lines in Figure 2) corresponds to hematite α-Fe_2O_3. Hematite is rather well crystallized with the narrowest spectral lines for the studied sample, $0.30 \leq W \leq 0.35$ mm s^{-1}. Small quadrupole splitting QS = 0.21 mm s^{-1} indicates a slight distortion of the iron local environment in the rhombohedral α-Fe_2O_3 lattice. The hyperfine interaction parameters of the two remaining sextets are similar to those in magnetite Fe_3O_4. Pure magnetite crystallizes in the inverse spinel structure in which Fe^{2+} and Fe^{3+} ions are distributed over tetrahedral A and octahedral B sites: $(Fe^{3+})_A(Fe^{2+}Fe^{3+})_BO_4$. Tetrahedral Fe^{3+} ions exhibit a magnetically split pattern with H_{eff} = 49.4 T (blue lines in Figure 2). A fast electronic exchange at room temperature between octahedral Fe^{2+} and Fe^{3+} ions compared to ^{57m}Fe nuclear lifetime ($t_{1/2}$ = 100 ns) does not allow one to distinguish two different iron oxidation states in magnetite. Consequently, the average Zeeman pattern with intermediate IS between limiting values of Fe^{3+} (0.37 mm s^{-1}) and Fe^{2+} (1.0 mm s^{-1}) is observed. Magnetite is clearly ill-crystallized and impure. Both A and B sites are disordered, characterized by large line widths: $0.38 \leq W_A \leq 0.54$ mm s^{-1}, and $0.7 \leq W_B \leq 2.1$ mm s^{-1}. In particular, the B-sublattice appears to be highly disordered, suggesting a partial occupation of iron sites by metallic cations of similar size (Mn^{2+}, Ca^{2+}, etc.). The most intense quadrupole doublet (47.7% of the total resonance pattern) corresponds to high-spin Fe^{3+} species in oxide environment. Similar hyperfine interaction parameters are observed for a number of highly dispersed pure and mixed iron oxides and hydroxides. The absence of magnetic ordering at room temperature suggests the average size of iron

oxide particles to be below 10 nm. An increased line width for the quadrupole doublet (0.50 mm s^{-1}) is consistent with this hypothesis.

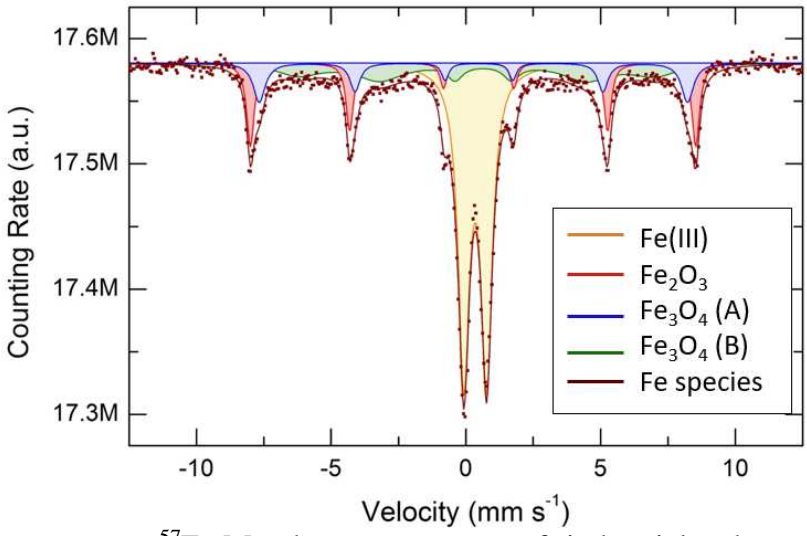

Figure 2: Room-temperature ^{57}Fe-Mössbauer spectrum of industrial ash sample measured in absorption geometry. Red square dots are the experimental measurements and coloured lines result from the deconvolution procedure.

2.5. Iron concentration and isotope measurements

The filtered solutions obtained from the industrial ash dissolution experiments were evaporated at 120ºC, re-dissolved in 2 ml of conc. sub-boiled HNO_3 and dried at 120ºC. The final residues were subsequently solubilized by 1 mL of sub-boiled 6M HCl and stored in the refrigerator until Fe purification through anion exchange chromatography in an HCl medium took place. The Fe purification procedure used 1.6 ml of Bio-Rad AG1 X-8, 100-200 mesh resin loaded in Bio-Rad Poly-Prep columns, both cleaned with 6M sub-boiled HCl, 1M sub-boiled HNO_3 and ultrapure water (≥18.2 MΩ cm). The cleaned resins were preconditioned with 10 ml of 6M sub-boiled HCl, prior to the introduction of 2 ml of the sample previously dissolved in 6M sub-boiled HCl. The matrix was eluted in 30 ml of 6M sub-boiled HCl, whereas the Fe was collected with 20 ml of 0.5M sub-boiled HCl. The solutions containing the purified Fe were dried and re-dissolved with sub-boiled 0.05M HNO_3 for Fe isotope measurements.

Iron isotope measurements were carried out at the Université Libre de Bruxelles (Laboratoire G-Time) with a Nu Plasma II Multi-Collector Inductively Coupled Plasma Mass Spectrometer (MC-ICP-MS) from Nu Instruments (Wrexham, UK). An Aridus-II desolvating sample introduction system from Cetac Technologies was used to reduce the predominant $^{40}Ar^{14}N$, $^{40}Ar^{16}O$ and $^{40}Ar^{16}O^{1}H$ interferences on iron isotopes 54, 56 and 57, respectively. The instrument was further operated in pseudo-high-resolution mode (R ~ 1600), to partially resolve the abovementioned polyatomic argon-based interferences from the Fe masses. This is achieved by reducing the width of the source-defining slit using a selectable slit mechanism and then reducing the width of the alpha slit located before the ESA (Electrostatic Analyzer) to enhance the peak shape by reducing any image aberration, resulting in a flat-topped section of resolved peak for isotopic ratio measurements (Figure S1). In addition to the Fe masses, ^{53}Cr was also monitored and an online Cr correction was applied to account for any iso-baric interference from ^{54}Cr on mass ^{54}Fe. This correction was either negligible or non-existent due to the effective separation of Fe from Cr during column chemistry.

Instrumental mass bias was corrected by external normalization with Ni added to standards and samples, applying the exponential law in combination with standard-sample bracketing. Both sample and standard solutions were run at 1 ppm Fe doped with 1 ppm Ni in 0.05M HNO_3, giving a total Fe beam intensity of ~ 25V and a total Ni beam intensity of ~ 20V. Two isotopic ratios were measured ($^{56}Fe/^{54}Fe$, $^{57}Fe/^{54}Fe$) in the analytical sessions, but only $^{56}Fe/^{54}Fe$ ratios were reported since samples plot on a single mass dependent fractionation line. The results are reported using delta notation relative to international Fe standard IRMM-014 (European Commission Institute for Reference Materials and Measurements), as described by Equation 1.

$$\delta^{56}Fe\ (‰) = [(^{56}Fe/^{54}Fe)_{sample} / (^{56}Fe/^{54}Fe)_{IRMM14} - 1\ ]\times 10^{3} \quad \text{(Eq. 1)}$$

Accuracy and reproducibility were assured by analyzing an in-house quality control standard called “MIX”. The MIX standard contains Fe extracted and purified by ion chromatography from Ammonitico Rosso carbonates (Préat et al., 2008). The $\delta^{56}Fe$ values found herein for the in-house

MIX standard was -1.58 ± 0.10‰ (2SD, n = 5), in agreement with the long-term measurement average value obtained on this instrument (Table S5). The accuracy of the MIX in-house standard reference material had been verified prior to this study by concomitant analysis of two reference materials from the Swiss Federal Institute of Technology (ETH, Zürich) with well-established consensus values: ETH Hematite and ETH Fe Salt. Our results (Table S5) were in good agreement with the reported values from expert laboratories equipped with various types of MC-ICP-MS instruments (Dideriksen et al., 2008; Teutsch et al., 2005; Williams et al., 2004; Poitrasson and Freydier, 2005).

The magnitude of the isotope fractionation ($\Delta^{56}Fe_{solution\text{-}bulk\ ash}$) was calculated using Equation 2 by comparing the Fe isotope compositions of the solutions with the initial bulk industrial ash, as also proposed by Wiederhold et al. (2006). The isotope composition of the industrial ash used herein was first measured and reported by Maters et al. (2017) with a $\delta^{56}Fe$ value of -0.12 ± 0.08‰.

$$\Delta^{56}Fe_{solution\text{-}bulk\ ash} = \delta^{56}Fe_{solution} - \delta^{56}Fe_{buk\ ash} \qquad \text{(Eq. 2)}$$

3. RESULTS AND DISCUSSION

3.1. Ash particle composition

The industrial ash collected from a Fe-Mn alloy company consists of a mixture of metallic, aluminosilicate, and, mainly, of internally mixed "aluminosilicate-metallic" particles (Marris et al. 2012 and Marris et al. 2013). Mössbauer measurements shown herein evidenced the presence of α-hematite and magnetite particles (Fig. 2), also shown by automated SEM-EDX analyses performed by Marris et al. (2013). But, in relation to their size, 44 to 60% of the analyzed particles consist of an internal mixture of aluminosilicates with Fe- and Mn-oxides (e.g., hausmannite, bixbyite). The high-spin Fe^{3+} species in an oxide environment, evidenced in Mössbauer measurements (section 2.5), responsible for the most intense quadrupole doublet (Figure 2), are linked with a heterogeneous metal distribution inside these particles. In summary, the most prevalent Fe-rich particle type in ash

(up to 60%), consist of a set of poorly crystallized manganoferrite nanoparticles, with a grain size up to 10 nm, that could explain the most intense Mössbauer signal. A detailed interpretation and discussion of the Mössbauer analysis are available in the Supplementary Material.

3.2. Dissolved iron isotope composition

Dissolved iron average concentrations increased from 155 to 397 µg/L from 5 to 120 min, which represents a solubility ranging from 1 to 2.5% (Figure 3a and Table S6). The dissolution process of the industrial ash as a function of time (Figure 3b) can be divided into two stages based on the dissolved Fe isotopic composition (δ^{56}Fe), i.e.: (*i*) early-stage dissolution (until 60 min), and (*ii*) late-stage dissolution (after 60 min), as also proposed by Wiederhold et al. (2006) during the dissolution of goethite under controlled experimental conditions. In the early stage, the preferential dissolution of light Fe isotopes occurs, with a minimum measured $\delta^{56}Fe_{solution}$ value of -0.45 ± 0.07‰ at 5 minutes dissolution time. As the dissolution contact time increases, Fe isotope composition becomes heavier, toward the values of the bulk industrial ash (i.e., -0.12 ± 0.08‰, Maters et al., 2017). At the late-stage dissolution, dissolved Fe isotope composition becomes heavier than the bulk industrial ash, achieving a measured $\delta^{56}Fe_{solution}$ value of +0.09± 0.07‰ at maximum Fe dissolution.

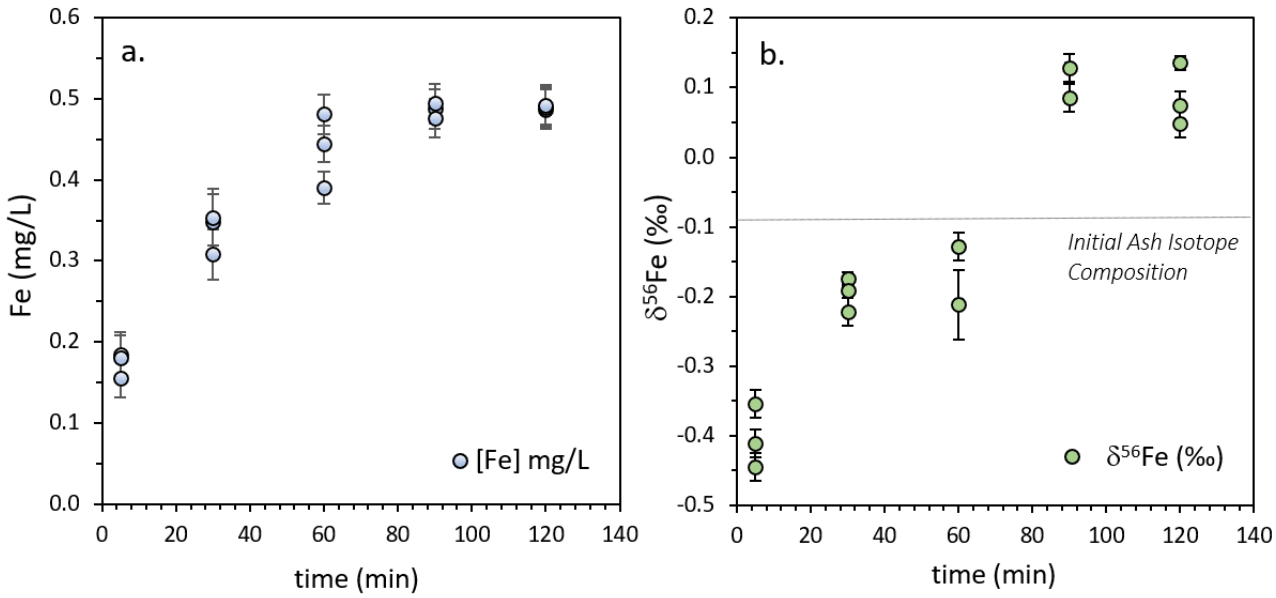

Figure 3: (a) Dissolved Fe concentration and (b) isotopic composition during dissolution experiments of the industrial ash. The horizontal dashed line corresponds to the initial ash isotope composition ($\delta^{56}Fe_{bulk\ ash}$).

3.3. Mechanism controlling dissolved iron isotope fractionation

To evaluate the extent to which the kinetic isotope effect controls the evolution of the dissolved Fe isotope composition, the experimental $\Delta^{56}Fe_{solution\text{-}bulk\ ash}$ data were compared with the Wiederhold's kinetic effect model (Wiederhold et al., 2006). This empirical model has been well applied to explain the early-stage dissolution process within one surface monolayer of Fe-bearing minerals in which the preferential depletion of isotopically light Fe occurs. Density Functional Theory (DFT) provides an alternative to empirical models to explain observed fractionations. However, when applied to the same system studied by Wiederhold et al. (2006), i.e. goethite dissolution in oxalate aqueous solutions, these DFT predictions resulted in significant disagreement as to the magnitude of the fractionation reached at equilibrium ($1.91<\Delta^{56}Fe_{solution\text{-}goethite}<2.18$‰, vs. ≅ 0.30‰ for experimental measurements (Domagal-Goldman and Kubicki, 2008)). Furthermore, the DFT results do not give any information on the temporal evolution of the fractionation and we have therefore chosen the empirical model of Wiederhold to guide our interpretation of the experimental results obtained here. A detailed description of our calculations is provided in Appendix A and model outputs are presented

in Figure 4b. Two fitting parameters are used, i.e.: (*i*) the fractionation constant, converted to the enrichment factor ε (Wiederhold et al., 2006); and (*ii*) the surface site density of Fe atoms (SSD – see Appendix A), used in the calculation of the fraction of iron atoms (ρ, in % of the total number of Fe atoms) that belong to the reactive surface site pool (rss).

In the early-stage dissolution (Fig. 3), the maximum Fe isotope fractionation was observed at 5 min with a $\Delta^{56}Fe_{solution\text{-}bulk\ ash}$ of -0.28 ± 0.10‰, whereas in the late-stage dissolution the maximum Fe isotope fractionation occurred at 90 min with a $\Delta^{56}Fe_{solution\text{-}bulk\ ash}$ of +0.23 ± 0.09‰. Applying the kinetic isotope effect model to the experimental data (Figure 4b), the best fit was obtained for a SSD of 2 sites/nm^2, close to the minimum value proposed by Koretsky et al. (1998) for pure crushed hematite (4.5 sites/nm^2). It results in a fraction of Fe atoms that belongs to the reactive surface site ρ = 0.22%, and an enrichment factor $\varepsilon = -1‰$, close to the value of -1.7‰, corresponding to the best fit value for the $^{56}Fe/^{54}Fe$ data obtained for goethite by Wiederhold et al. (2006).

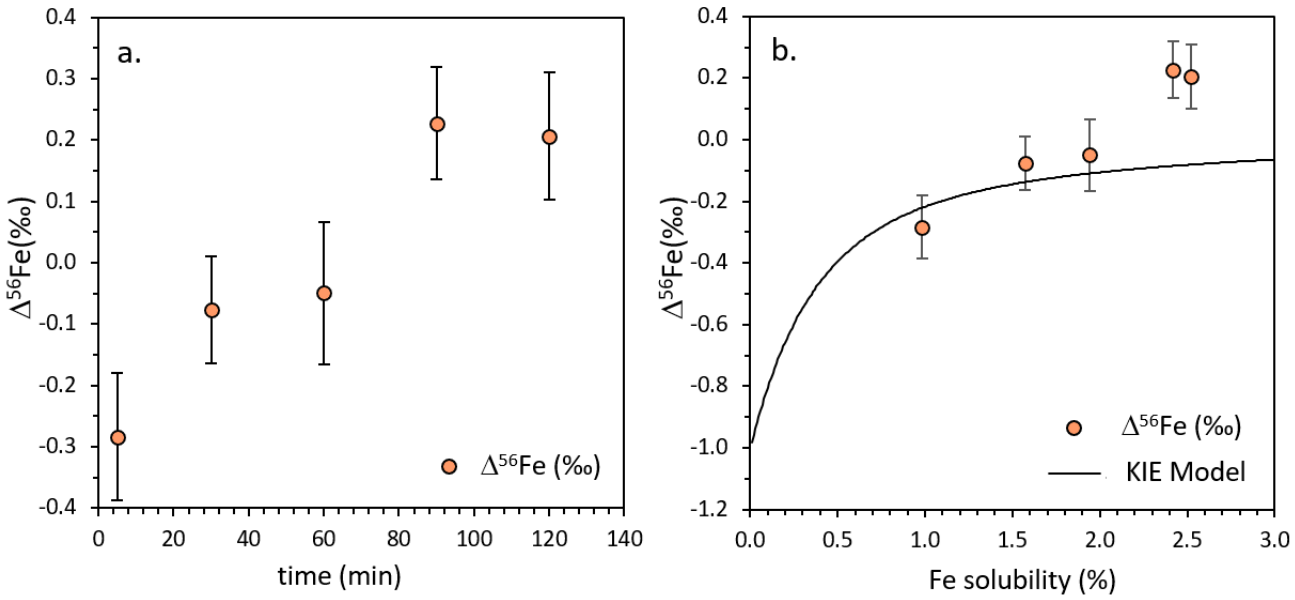

Figure 4: (a) Variation of Fe isotope fractionation over ash-solution contact time periods at room temperature, with UV/VIS irradiation ($\Delta^{56}Fe$ is reported relative to the bulk ash – Eq. 2). (b) Kinetic Isotope Effect (KIE) Model output *vs.* experimental data (± 2 S.D. reported as error bars) obtained for isotope fractionation during industrial-ash dissolution in cloud water simulation experiments

347 The model succeeded in describing the kinetic-controlled isotope fractionation process at the
348 early-stage dissolution of Fe-bearing aerosols in which the faster breakage of energetically weaker
349 ^{54}Fe-O surface bonds occurs, but it was not able to describe the late-stage dissolution due to near-
350 equilibrium conditions in which equilibrium isotope effects prevail. The good agreement between the
351 experimental data found during the early-stage dissolution and the model data suggests that kinetic
352 isotope effect is a significant mechanism controlling the isotope signatures of dissolved Fe during the
353 atmospheric processing of an anthropogenic aerosol. However, Revels et al. (2015) showed that an
354 argumentation based on a simple data fit to a kinetic isotope effect model is not robust enough to
355 suggest kinetic isotope fractionation as the only mechanism controlling the isotopic evolution of the
356 δ^{56}Fe values over time. These authors showed that the evolution of dissolved Fe isotope composition
357 over ash and solution contact time periods can be attributed to (i) the mixing of leached fractions
358 from two phases (i.e., poorly and well crystallized Fe oxides) yielding different labilities and isotope
359 compositions without isotope fractionation of either phases, according to a two-phases mixing
360 model; and (ii) a kinetic-controlled isotope fractionation due to the faster breakage of ^{54}Fe-O bonds
361 from Fe oxides on the ash surface, according to a kinetic isotope effect model, highlighting the
362 complexity of determining the mechanism controlling the leached δ^{56}Fe values evolution during ash
363 dissolution by cloud processing.

364 Analyzing the isotopic composition of each separate Fe phase (i.e., poorly and well crystallized
365 Fe oxides) can be an attractive approach for evidencing if the two-phases mixing process is an
366 important mechanism controlling the evolution of dissolved Fe and δ^{56}Fe values. However, there is a
367 lack of consensus on the appropriate method for extracting the reactive phase for Fe isotope
368 determination (Chen et al., 2020), especially for the extraction of poorly crystallized and amorphous
369 Fe oxides. The most efficient selective methods for the separation of poorly-crystallized and
370 amorphous Fe oxides are the ascorbic acid (Raiswell et al., 2010) and hydroxylamine hydrochloride
371 (Berger et al., 2008) methods. However, they also induce Fe kinetic and equilibrium isotope effects

through ligand and proton promoted dissolution and redox reactions according to particle mineral assemblage composition (Brantley et al., 2004; Wiederhold et al., 2006; Chapman et al., 2009; Kiczka et al., 2010). Information on the isotope composition differences between poorly and well crystalized oxides should come from a different approach. For instance, Flament et al. (2008) showed that the high-temperature sintering operation tends to standardize the isotope composition of the Fe phases presented therein, since the collected dust had δ^{56}Fe values ranging only from +0.53 to +0.86 ‰, which are much more homogeneous than the ore used in the sintering process (δ^{56}Fe values ranging only from -0.16 to +1.19). The referred work was carried out in a steel industry close to the one in which the dust was collected by the present study, both with same sintering process (e.g., temperature, ores, and reducing and melting agents). Additionally, Chen et al. (2020) showed that differences between Fe isotope signatures of amorphous Fe (hydro)oxides, ferrihydrite, and more crystallized goethite and hematite are small, based on the homogeneity of the isotopic signatures generally observed for dust Fe mineral phases, despite the high variability of the poorly and well crystalized Fe oxides concentrations. Therefore, a two-phases mixing process may not be so relevant to explain the evolution of Fe isotope composition found herein, since the differences of the Fe isotope composition of such particles are small, irrespective of their crystallinity. Therefore, kinetic isotope effects are likely to be the most important process controlling the evolution of δ^{56}Fe values over time during ash dissolution.

3.4. Mechanisms of Fe isotope fractionation during cloud processing

The good agreement of the experimental data with the kinetic fractionation model shows the faster release of ^{54}Fe at the onset of the ligand-controlled dissolution process, due to the faster breakage of the ^{54}Fe-O surface bond, by comparison with bonds involving heavier isotopes, as it is generally accepted on a theoretical basis (Schauble et al., 2001). Ligand-controlled dissolution occurs through the formation of strong surface complexes, which weaken the bonds between Fe atoms and

397 the coordinating oxygen atoms in the particle lattice surface (Stumm, 1995). This process is prone to
398 cause significant isotope fractionation, due to the faster breakage of the energetically weaker ^{54}Fe-O
399 bond, forming aqueous species such as $Fe(C_2O_4)_n$ due to the presence of oxalate. Previous studies
400 showed that ligand-controlled dissolution causes Fe isotope fractionation of goethite, granite, basalts
401 and phyllosilicates in experiments containing oxalic acid (Wiederhold et al., 2006; Chapman et al.,
402 2009). Organic ligands also promote ligand-to-metal electron transfer in the organo-Fe(III) surface
403 complexes under the irradiation of UV/VIS light, causing Fe solubilization as aqueous Fe(II) species
404 (Chen and Grassian, 2013). This process, known as reductive ligand-promoted dissolution, can also
405 cause isotope fractionation of Fe oxides with a measured $\Delta^{56}Fe_{solution\text{-}goethite}$ of -1.67‰. Conversely,
406 previous studies investigating Fe dissolution from hematite and ferromanganese nodules showed that
407 proton-promoted dissolution has a limited effect on Fe isotope fractionation, although known as the
408 most important process to cause Fe oxides dissolution in acidic conditions, due to the breakage of Fe-
409 O lattice bonds, during protonation of oxyhydroxides surface sites.

410 The role of organic ligands in Fe dissolution is also evidenced at the late-stage dissolution, in
411 which equilibrium isotope effects are observed. The depletion in ^{54}Fe of the leached layer leads to the
412 breaking of higher energy bonds and to the relative ^{56}Fe enrichment of the solution, inducing lower
413 isotope fractionation rates, on the time scale considered here. For dissolved Fe fractions > 2% an
414 enrichment of the cloud water in ^{56}Fe ($\Delta^{56}Fe > 0$) is even observed. Wiederhold et al. (2006),
415 concluded that such results confirmed ligand-controlled dissolution processes, giving rise to the
416 formation in solution of Fe-complexes, with a strong bond energy. Even if the leached solid surface
417 layer becomes enriched in heavy Fe isotopes, these Fe-O bonds are weaker than bonds existing in
418 aqueous Fe-complexes leading to heavy Fe isotopes enrichment in the solution.
419

420 ## 4. IMPLICATIONS

421 The present study is part of current attempts to improve geochemical models of anthropogenic
422 Fe aerosols deposition to the oceans. It is based on a simplified description of the phenomena taking
423 place during the incorporation of pyrogenic particles within the cloud masses. The results presented
424 herein showed that atmospheric processing of pyrogenic particles, as an industrial ash, can generate
425 Fe isotope fractionation with different magnitudes and directions, according to the ash solution
426 contact time (i.e., atmospheric processing time scale) and the fraction of Fe dissolved from the
427 airborne particles. This indicates that atmospheric processes and especially the incorporation of the
428 particles within the cloud masses, complicate the analysis of the origin of the iron aerosols, in the
429 sense that the partial solubilization of these particles induces an Fe isotope fractionation of variable
430 extent. If the particles are dry deposited near the sources, in the epicontinental oceanic zones, the
431 initial soluble Fe isotopically light signatures of anthropogenic particles are probably preserved. On
432 the other hand, if the residence time within the troposphere is longer, as shown by Rodríguez et al.
433 (2021), the solubility of iron increases with the multiplication of evaporation and condensation
434 cycles (atmospheric processing). Iron fractional dissolution undergone during different atmospheric
435 processing time scales may release Fe with contrasted isotope compositions (Fig. 4) to solution,
436 changing the original soluble Fe isotope signature (which is linked to its source). This might be
437 especially important when the dissolution process goes from kinetic to near-equilibrium conditions,
438 in which higher amounts of Fe are progressively released from ash surface. These findings shows
439 that it is then necessary to be able to distinguish between what comes from short-term atmospheric
440 processes (on the scale of the lifetime of a cloud droplet) and what is part of longer processes, since
441 the impact of atmospheric processing on soluble Fe isotope compositions can be significant. The
442 different behavior of natural dust, less soluble and therefore less sensitive to the effect of
443 atmospheric processing, will likely facilitate the determination of their isotopic signature at the time
444 of their oceanic deposition. However, this observation must be relativized when the atmospheric
445 residence time of these dust increases, since it increases the possibility that they are mixed with

pyrogenic particles within the cloud droplets, which should lead to an increase of their solubility. The situation will be different for pyrogenic particles, because of their highly variable initial solubility, depending on the source considered (Rodríguez et al., 2021 and references therein) and also because of their greater sensitivity to atmospheric processes. Conclusively, despite the simplifications intrinsic to laboratory studies, the fractionations measured here are consistent with those obtained on real aerosols by Conway et al. (2019), results that allowed these authors to refine the quantification of soluble iron deposition to the oceans. The present study shows that cloud processing should be considered and investigated while using δ^{56}Fe values to constrain anthropogenic and natural Fe in near-source and open-ocean aerosols, and, ultimately when it comes to defining the isotopic composition of the atmospheric source term, in studies concerned with the identification of processes and fluxes of key elements in ocean biogeochemistry, as well as their evolution in response to changes in climatic and environmental conditions. Other studies evaluating the effects of cloud processing on Fe isotope fractionation are highly encouraged, especially those performed at lower dust concentrations (which better represents the concentrations commonly found in cloud water), since it effects Fe solubility and might play an important role controlling the magnitude of the Fe isotope fractionation.

Acknowledgements

LPCA acknowledge financial support from the CaPPA (Chemical and Physical Properties of the Atmosphere) project funded by the French National Research Agency (ANR), through the PIA (Programme d'Investissement d'Avenir) under contract ANR-11-LABX-0005-01, and from the CPER project CLIMIBIO, funded by the French Ministry of Higher Education and Research, the CNRS, the Regional Council “Hauts-de-France” and the European Regional Development Fund (ERDF). The authors thanks the two anonymous reviewers for their comments, which allowed us to substantially improve the manuscript. The authors also thank Elena Charlene Maters for preliminary

solubilization procedures under UV/VIS irradiation, as well as the first iron purification protocols. Dorothée Dewaele is also acknowledged for supporting Fe concentration measurements.

APPENDIX A

Our simulation of the behavior of iron isotopes during the dissolution of Fe-bearing particles is based on the description of the kinetic fractionation model developed in the Supporting Information in Wiederhold et al.(Wiederhold et al., 2006). The model distinguishes the iron atoms according to their atomic mass number $A \in \{54,56,57,58\}$ and is based on their location: in the bulk mineral, in its reactive surface site (*rss*) pool or in the solution surrounding the mineral. The number of ${}^{A}_{26}Fe$ atoms in solution is labeled $N_{solution}^{Fe-A}$ with equivalent notations for the bulk and the *rss* pool. The total number of iron atoms in solution is $N_{solution}^{Fe-*} = N_{solution}^{Fe-54} + N_{solution}^{Fe-56} + N_{solution}^{Fe-57} + N_{solution}^{Fe-58}$ and N_{tot} is the total number of iron atoms in the system. The reaction progress variable is defined as the number of iron atoms in solution:$\xi = N_{solution}^{Fe-*}$, and the dissolved fraction is equal to:$100\frac{N_{solution}^{Fe-*}}{N_{tot}}$ (in %). The fraction of a given isotope *A* in the mineral before dissolution is X_A.

According to Wiederhold et al.(Wiederhold et al., 2006), the evolution of the number of iron isotopes in the reactive surface site pool is driven by two contributions:

$$\frac{dN_{rss}^{Fe-A}}{d\xi} = -\frac{(1+f_A)N_{rss}^{Fe-A}}{(1+f_{54})N_{rss}^{Fe-54}+(1+f_{56})N_{rss}^{Fe-56}+(1+f_{57})N_{rss}^{Fe-57}+(1+f_{58})N_{rss}^{Fe-58}} + \left(1-\frac{N_{solution}^{Fe-*}}{N_{tot}}\right)X_A. \quad \text{(A1)}$$

The first term on the right-hand side of the equation is the contribution of iron atoms moving with isotope fractionation from the rss pool to the solution, while the second term describes iron atoms going from the bulk to the rss pool without any fractionation. If a fixed percentage of atoms in the mineral goes from the bulk to the rss pool during the dissolution, it is expected that the number of atoms arriving to the *rss* pool decreases with time, this is modeled via the coefficient $\left(1-\frac{N_{solution}^{Fe-*}}{N_{tot}}\right)$ in front of X_A. The coefficients f_n(for example): $f_{56} = \frac{md_{56}}{1000(md_{56}-md_{54})}\epsilon$) depend on the enrichment factor ϵ (ϵ in ‰). The constants

494 md_n are the mass differences for the iron isotopes relative to that of natural Fe and are tabulated in Table
495 S3 (IRMM-014) of the Supporting Information in Wiederhold et al.(Wiederhold et al., 2006).

496 We extend the set of differential equations of Wiederhold et al.(Wiederhold et al., 2006) by considering
497 the evolution of the number of iron isotopes in the solution as well:

498 $$\frac{dN_{solution}^{Fe-A}}{d\xi} = \frac{(1+f_A)N_{rss}^{Fe-A}}{(1+f_{54})N_{rss}^{Fe-54}+(1+f_{56})N_{rss}^{Fe-56}+(1+f_{57})N_{rss}^{Fe-57}+(1+f_{58})N_{rss}^{Fe-58}}. \quad \text{(A2)}$$

499

500 The fraction of iron atoms (ρ, in%) that belong to the reactive surface site pool is

501 $$\rho = 100.SSD.SA.M_{mineral}/N_A \quad \text{(A3)}$$

502 where: (i) $SA = 3.7\ m^2/g$ is the measured (B.E.T. method) surface area of the industrial ash (table S1 in SI);
503 (ii) $N_A = 6.02.10^{23}\ mol^{-1}$is the Avogadro number; (iii) $SSD = 2\ sites/nm^2$ is the surface site density of
504 iron atoms, based on the range of values proposed by Koretsky et al.(Koretsky et al., 1998) for crushed
505 hematite; and (iv) $M_{mineral} = 177.14\ g/mol$ is the *ash equivalent molar mass*, obtained from a linear
506 combination of the molar masses of pure phases identified from X-ray diffraction and Mössbauer
507 spectroscopy measurements (sections 2.5 and 3.1). The contributions of pure phases are arbitrarily set to 20
508 wt.% for α-Fe_2O_3 (M = 159.69 g/mol), 25 wt.% for Fe_3O_4 (M = 231.50 g/mol) and 55 wt.% for $FeMnO_3$ (158.78
509 g/mol).

510 With the above values we obtain $\rho = 0.22\%$.

511 Initially, there are no atoms in the solution and the vector of initial conditions is:

$$\begin{pmatrix} N_{rss}^{Fe-54}(0) \\ N_{rss}^{Fe-56}(0) \\ N_{rss}^{Fe-57}(0) \\ N_{rss}^{Fe-58}(0) \\ N_{solution}^{Fe-54}(0) \\ N_{solution}^{Fe-56}(0) \\ N_{solution}^{Fe-57}(0) \\ N_{solution}^{Fe-58}(0) \end{pmatrix} = \frac{\rho}{100} N_{tot} \begin{pmatrix} X_{54} \\ X_{56} \\ X_{57} \\ X_{58} \\ 0 \\ 0 \\ 0 \\ 0 \end{pmatrix}. \quad (512)$$

We arbitrarily choose $N_{tot} = 10000$ to numerically solve the system of coupled differential equations with Maple 2019 and compute $\delta^{56}Fe_{solution}(\xi)$ as:

$$\delta^{56}Fe_{solution}(\xi) = 1000 \left(\frac{\frac{N_{solution}^{Fe-56}(\xi)}{N_{solution}^{Fe-54}(\xi)}}{\frac{X_{IRMM}^{Fe-56}}{X_{IRMM}^{Fe-54}}} - 1 \right). \quad (516)$$

We then obtain $\Delta^{56}Fe_{solution}(\xi)$ through the relation $\Delta^{56}Fe_{solution}(\xi) = \delta^{56}Fe_{solution}(\xi) + 0.12‰$.

REFERENCES

Beard, B., 2003. Application of Fe isotopes to tracing the geochemical and biological cycling of Fe. Chem. Geol. 195, 87–117. https://doi.org/10.1016/S0009-2541(02)00390-X

Berger, C.J.M., Lippiatt, S.M., Lawrence, M.G., Bruland, K.W., 2008. Application of a chemical leach technique for estimating labile particulate aluminum, iron, and manganese in the Columbia River plume and coastal waters off Oregon and Washington. J. Geophys. Res. 113, 1–16. https://doi.org/10.1029/2007jc004703

Boyd, P.W., Ellwood, M.J., 2010. The biogeochemical cycle of iron in the ocean. Nat. Geosci. 3, 675–682. https://doi.org/10.1038/ngeo964

Chapman, J.B., Weiss, D.J., Shan, Y., Lemburger, M., 2009. Iron isotope fractionation during leaching of granite and basalt by hydrochloric and oxalic acids. Geochim. Cosmochim. Acta 73, 1312–1324. https://doi.org/10.1016/j.gca.2008.11.037

Chen, H., Grassian, V.H., 2013. Iron dissolution of dust source materials during simulated acidic processing: The effect of sulfuric, acetic, and oxalic acids. Environ. Sci. Technol. 47, 10312–10321. https://doi.org/10.1021/es401285s

Chen, T., Li, W., Guo, B., Liu, R., Li, G., Zhao, L., Ji, J., 2020. Reactive iron isotope signatures of the East Asian dust particles: Implications for iron cycling in the deep North Pacific. Chem. Geol. 531, 119342. https://doi.org/10.1016/j.chemgeo.2019.119342

538 Conway, T.M., Hamilton, D.S., Shelley, R.U., Aguilar-Islas, A.M., Landing, W.M., Mahowald,
539 N.M., John, S.G., 2019. Tracing and constraining anthropogenic aerosol iron fluxes to the North
540 Atlantic Ocean using iron isotopes. Nat. Commun. 10, 1–10. https://doi.org/10.1038/s41467-
541 019-10457-w

542 Conway, T.M., John, S.G., 2014. Quantification of dissolved iron sources to the North Atlantic
543 Ocean. Nature 511, 212–215. https://doi.org/10.1038/nature13482

544 Dideriksen, K., Baker, J. a., Stipp, S.L.S., 2008. Equilibrium Fe isotope fractionation between
545 inorganic aqueous Fe(III) and the siderophore complex, Fe(III)-desferrioxamine B. Earth Planet.
546 Sci. Lett. 269, 280–290. https://doi.org/10.1016/j.epsl.2008.02.022

547 Domagal-Goldman, S.D., Kubicki, J.D., 2008. Density functional theory predictions of equilibrium
548 isotope fractionation of iron due to redox changes and organic complexation. Geochim.
549 Cosmochim. Acta 72, 5201–5216. https://doi.org/10.1016/j.gca.2008.05.066

550 Field, C.B., Behrenfeld, M.J., Randerson, J.T., Field, C.B., Behrenfeld, M.J., Randerson, J.T., 1998.
551 Primary Production of the Biosphere : Integrating Terrestrial and Oceanic Components
552 Published by : American Association for the Advancement of Science Stable URL :
553 http://www.jstor.org/stable/2896014 Linked references are available on JSTOR for this arti.
554 Science (80-.). 281, 237–240.

555 Flament, P., Mattielli, N., Aimoz, L., Choël, M., Deboudt, K., Jong, J. de, Rimetz-Planchon, J.,
556 Weis, D., 2008. Iron isotopic fractionation in industrial emissions and urban aerosols.
557 Chemosphere 73, 1793–1798. https://doi.org/10.1016/j.chemosphere.2008.08.042

558 Flossmann, A.I., Wobrock, W., 2019. Cloud processing of aerosol particles in marine stratocumulus
559 clouds. Atmosphere (Basel). 10. https://doi.org/10.3390/atmos10090520

560 Geider, R.J., La Roche, J., 1994. The role of iron in phytoplankton photosynthesis, and the potential
561 for iron-limitation of primary productivity in the sea. Photosynth. Res. 39, 275–301.
562 https://doi.org/10.1007/BF00014588

563 Guo, J., Wang, Y., Shen, X., Wang, Z., Lee, T., Wang, X., Li, P., Sun, M., Collett, J.L., Wang, W.,
564 Wang, T., 2012. Characterization of cloud water chemistry at Mount Tai, China: Seasonal
565 variation, anthropogenic impact, and cloud processing. Atmos. Environ. 60, 467–476.
566 https://doi.org/10.1016/j.atmosenv.2012.07.016

567 Ito, A., Myriokefalitakis, S., Kanakidou, M., Mahowald, N.M., Scanza, R.A., Hamilton, D.S., Baker,
568 A.R., Jickells, T., Sarin, M., Bikkina, S., Gao, Y., Shelley, R.U., Buck, C.S., Landing, W.M.,
569 Bowie, A.R., Perron, M.M.G., Guieu, C., Meskhidze, N., Johnson, M.S., Feng, Y., Kok, J.F.,
570 Nenes, A., Duce, R.A., 2019. Pyrogenic iron: The missing link to high iron solubility in
571 aerosols. Sci. Adv. 5, eaau7671. https://doi.org/10.1126/sciadv.aau7671

572 Jickells, T.D., An, Z.S., Andersen, K.K., Baker, A.R., Bergametti, G., Brooks, N., Cao, J.J., Boyd,
573 P.W., Duce, R.A., Hunter, K.A., Kawahata, H., Kubilay, N., laRoche, J., Liss, P.S., Mahowald,
574 N., Prospero, J.M., Ridgwell, A.J., Tegen, I., Torres, R., 2005. Global Iron Connections
575 Between Desert Dust, Ocean Biogeochemistry, and Climate. Science (80-.). 308, 67 LP – 71.
576 https://doi.org/10.1126/science.1105959

577 Johansson, G., Yokoyama, H., 1990. Inner- and outer-sphere complex formation in aqueous erbium
578 halide and perchlorate solutions. An x-ray diffraction study using isostructural substitution.
579 Inorg. Chem. 29, 2460–2466. https://doi.org/10.1021/ic00338a015

580 Kiczka, M., Wiederhold, J.G., Frommer, J., Kraemer, S.M., Bourdon, B., Kretzschmar, R., 2010.

Iron isotope fractionation during proton- and ligand-promoted dissolution of primary phyllosilicates. Geochim. Cosmochim. Acta 74, 3112–3128. https://doi.org/10.1016/j.gca.2010.02.018

Kohfeld, K.E., Le Quéré, C., Harrison, S.P., Anderson, R.F., 2005. Role of marine biology in glacial-interglacial CO2 cycles. Science (80-.). 308, 74–78. https://doi.org/10.1126/science.1105375

Koretsky, C.M., Sverjensky, D.A., Sahai, N., 1998. A model of surface site types on oxide and silicate minerals based on crystal chemistry; implications for site types and densities, multi-site adsorption, surface infrared spectroscopy, and dissolution kinetics. Am. J. Sci. 298, 349–348.

Kurisu, M., Sakata, K., Miyamoto, C., Takaku, Y., Iizuka, T., Takahashi, Y., 2016a. Variation of Iron Isotope Ratios in Anthropogenic Materials Emitted through Combustion Processes. Chem. Lett. 45, 970–972. https://doi.org/10.1246/cl.160451

Kurisu, M., Takahashi, Y., Iizuka, T., Uematsu, M., 2016b. Very low isotope ratio of iron in fine aerosols related to its contribution to the surface ocean. J. Geophys. Res. Atmos. 121, 11038–11054. https://doi.org/10.1002/2016JD024957.Received

López-García, P., Gelado-Caballero, M.D., Patey, M.D., Hernández-Brito, J.J., 2021. Atmospheric fluxes of soluble nutrients and Fe: More than three years of wet and dry deposition measurements at Gran Canaria (Canary Islands). Atmos. Environ. 246. https://doi.org/10.1016/j.atmosenv.2020.118090

Luo, C., Mahowald, N., Bond, T., Chuang, P.Y., Artaxo, P., Siefert, R., Chen, Y., Schauer, J., 2008. Combustion iron distribution and deposition. Global Biogeochem. Cycles 22, 1–17. https://doi.org/10.1029/2007GB002964

Mahowald, N.M., Baker, A.R., Bergametti, G., Brooks, N., Duce, R.A., Jickells, T.D., Kubilay, N., Prospero, J.M., Tegen, I., 2005. Atmospheric global dust cycle and iron inputs to the ocean. Global Biogeochem. Cycles 19. https://doi.org/10.1029/2004GB002402

Majestic, B.J., Anbar, A.D., Herckes, P., 2009. Elemental and iron isotopic composition of aerosols collected in a parking structure. Sci. Total Environ. 407, 5104–5109. https://doi.org/10.1016/j.scitotenv.2009.05.053

Marris, H., Deboudt, K., Augustin, P., Flament, P., Blond, F., Fiani, E., Fourmentin, M., Delbarre, H., 2012. Fast changes in chemical composition and size distribution of fine particles during the near-field transport of industrial plumes. Sci. Total Environ. 427–428, 126–138. https://doi.org/10.1016/j.scitotenv.2012.03.068

Marris, H., Deboudt, K., Flament, P., Grobéty, B., Gieré, R., 2013. Fe and Mn oxidation states by TEM-EELS in fine-particle emissions from a Fe-Mn alloy making plant. Environ. Sci. Technol. 47, 10832–10840. https://doi.org/10.1021/es400368s

Martínez-Garcia, A., Rosell-Melé, A., Jaccard, S.L., Geibert, W., Sigman, D.M., Haug, G.H., 2011. Southern Ocean dust-climate coupling over the past four million years. Nature 476, 312–315. https://doi.org/10.1038/nature10310

Maters, E.C., Flament, P., de Jong, J., Mattielli, N., Deboudt, K., 2017. Investigating Changes in Iron Solubility and Isotopic Composition of Mineral Dust and Industrial Ash during Simulated Atmospheric Processing, in: 2017 AGU Fall Meeting. New Orleans, Louisiana, pp. 11–15.

Mead, C., Herckes, P., Majestic, B.J., Anbar, A.D., 2013. Source apportionment of aerosol iron in the marine environment using iron isotope analysis. Geophys. Res. Lett. 40, 5722–5727. https://doi.org/10.1002/2013GL057713

624 Paris, R., Desboeufs, K. V., 2013. Effect of atmospheric organic complexation on iron-bearing dust
625 solubility. Atmos. Chem. Phys. 13, 4895–4905. https://doi.org/10.5194/acp-13-4895-2013

626 Poitrasson, F., 2006. On the iron isotope homogeneity level of the continental crust. Chem. Geol.
627 235, 195–200. https://doi.org/10.1016/j.chemgeo.2006.06.010

628 Poitrasson, F., Freydier, R., 2005. Heavy iron isotope composition of granites determined by high
629 resolution MC-ICP-MS. Chem. Geol. 222, 132–147.
630 https://doi.org/10.1016/j.chemgeo.2005.07.005

631 Préat, A.R., De Jong, J.T.M., Mamet, B.L., Mattielli, N., 2008. Stable iron isotopes and microbial
632 mediation in red pigmentation of the Rosso Ammonitico (mid-late Jurassic, Verona area, Italy).
633 Astrobiology 8, 841–857. https://doi.org/10.1089/ast.2006.0035

634 Radic, A., Lacan, F., Murray, J.W., 2011. Iron isotopes in the seawater of the equatorial Pacific
635 Ocean: New constraints for the oceanic iron cycle. Earth Planet. Sci. Lett. 306, 1–10.
636 https://doi.org/10.1016/j.epsl.2011.03.015

637 Raiswell, R., Vu, H.P., Brinza, L., Benning, L.G., 2010. The determination of labile Fe in
638 ferrihydrite by ascorbic acid extraction: Methodology, dissolution kinetics and loss of solubility
639 with age and de-watering. Chem. Geol. 278, 70–79.
640 https://doi.org/10.1016/j.chemgeo.2010.09.002

641 Revels, B.N., Zhang, R., Adkins, J.F., John, S.G., 2015. Fractionation of iron isotopes during
642 leaching of natural particles by acidic and circumneutral leaches and development of an optimal
643 leach for marine particulate iron isotopes. Geochim. Cosmochim. Acta 166, 92–104.
644 https://doi.org/10.1016/j.gca.2015.05.034

645 Schauble, E.A., Rossman, G.R., Taylor, H.P., 2001. Theoretical estimates of equilibrium Fe-isotope
646 fractionations from vibrational spectroscopy. Geochim. Cosmochim. Acta 65, 2487–2497.
647 https://doi.org/10.1016/S0016-7037(01)00600-7

648 Sedwick, P.N., Sholkovitz, E.R., Church, T.M., 2007. Impact of anthropogenic combustion
649 emissions on the fractional solubility of aerosol iron: Evidence from the Sargasso Sea.
650 Geochemistry, Geophys. Geosystems 8. https://doi.org/10.1029/2007GC001586

651 Shi, Z., Krom, M.D., Jickells, T.D., Bonneville, S., Carslaw, K.S., Mihalopoulos, N., Baker, A.R.,
652 Benning, L.G., 2012. Impacts on iron solubility in the mineral dust by processes in the source
653 region and the atmosphere: A review. Aeolian Res. 5, 21–42.
654 https://doi.org/10.1016/j.aeolia.2012.03.001

655 Stumm, W., 1995. The Inner-Sphere Surface Complex, in: Chin Pao Huang, Charles R. O'Melia,
656 J.J.M. (Ed.), Aquatic Chemistry : Interfacial and Interspecies Processes. American Chemical
657 Society, San Francisco, pp. 1–32. https://doi.org/10.1021/ba-1995-0244.ch001

658 Tagliabue, A., Bopp, L., Dutay, J.C., Bowie, A.R., Chever, F., Jean-Baptiste, P., Bucciarelli, E.,
659 Lannuzel, D., Remenyi, T., Sarthou, G., Aumont, O., Gehlen, M., Jeandel, C., 2010.
660 Hydrothermal contribution to the oceanic dissolved iron inventory. Nat. Geosci. 3, 252–256.
661 https://doi.org/10.1038/ngeo818

662 Tagliabue, A., Bowie, A.R., Boyd, P.W., Buck, K.N., Johnson, K.S., Saito, M.A., 2017. The integral
663 role of iron in ocean biogeochemistry. Nature 543, 51–59. https://doi.org/10.1038/nature21058

664 Teutsch, N., von Gunten, U., Porcelli, D., Cirpka, O.A., Halliday, A.N., 2005. Adsorption as a cause
665 for iron isotope fractionation in reduced groundwater. Geochim. Cosmochim. Acta 69, 4175–
666 4185. https://doi.org/10.1016/j.gca.2005.04.007

667 Waeles, M., Baker, A.R., Jickells, T., Hoogewerff, J., 2007. Global dust teleconnections: Aerosol
668 iron solubility and stable isotope composition. Environ. Chem. 4, 233–237.
669 https://doi.org/10.1071/EN07013

670 Warneck, P., 1988. Chemistry of the natural atmosphere. Academic Press, San Diego, CA.

671 Wiederhold, J.G., Kraemer, S.M., Teutsch, N., Borer, P.M., Halliday, A.N., Kretzschmar, R., 2006.
672 Iron isotope fractionation during proton-promoted, ligand-controlled, and reductive dissolution
673 of Goethite. Environ. Sci. Technol. 40, 3787–93.

674 Wiesli, R.A., Beard, B.L., Johnson, C.M., 2004. Experimental determination of Fe isotope
675 fractionation between aqueous Fe(II), siderite and "green rust" in abiotic systems. Chem. Geol.
676 211, 343–362. https://doi.org/10.1016/j.chemgeo.2004.07.002

677 Williams, H.M., McCammon, C.A., Peslier, A.H., Halliday, A.N., Teutsch, N., Levasseur, S., Burg,
678 J.P., 2004. Iron isotope fractionation and the oxygen fugacity of the mantle. Science (80-.). 304,
679 1656–1659. https://doi.org/10.1126/science.1095679

680

681